Soft Matter, Issue 16, 2020, pp. 5020-5031
DOI: 10.1039/D0SM00315H

Effects of Eigen and Actual Frequencies of Soft Elastic Surfaces on droplet Rebound from Stationary Flexible Feather Vanes

Chengchun Zhang[a,b], Zhengyang Wu[a], Chun Shen[a,b]*, Yihua Zheng[a], Liang Yang[c], Yan Liu[a], Luquan Ren[a]

[a]*Key Laboratory of Engineering Bionics (Ministry of Education), Jilin University, Changchun 130022, China;*

[b]*State Key Laboratory of Automotive Simulation and Control, Jilin University, Changchun, 130022, China*

[c]*Centre for Renewable Energy Systems, Cranfield University, Cranfield, MK43 0AL, United Kingdom*

Abstract

The aim of this paper is to investigate the effect of eigenfrequency and the actual frequency of the elastic surface for the droplet rebound. The elastic surface used in this study is the stationary flexible feather vanes. A fluid-structure interaction (FSI) numerical model is proposed to predict the phenomenon, and later is validated by the experiment that the droplets impact the stationary flexible feather vanes. The effect of mass and stiffness of the surface is analysed. First, the suitable combination of mass and stiffness of the surface will enhance the drop rebound. Second, a small mass system with higher eigenfrequency will decrease the minimum contact time. In the last, the actual frequencies of the elastic surface, approximate at 75 Hz, can accelerate the drop rebound for all cases.

Keywords: eigenfrequency; actual frequency; droplet rebound; elastic surface; fluid-structure interaction(FSI); contact time.

1. Introduction

Droplets impact on a solid surface is a ubiquitous process that occurs in nature and in industrial processes[1-3]. Numerous studies have been focused on the wetting dynamics when droplets impact on different kinds of substrates, including macroscopically flat surfaces[4-9] or surfaces with a rough microstructure (pillar array, grooved texture, etc.)[10-19]. However, to date, most studies have been investigated droplets that impact on rigid surfaces.

In recent years, the impact of droplets on elastic or flexible natural surfaces, as well as artificial surfaces, has been examined. Unlike a stationary rigid surface, elastic or flexible substrates may exhibit changes in the wetting dynamics during the impact. Recent studies have been investigated the wetting dynamics of hydrophilic flexible substrates[20-23]. Typically, flexible hydrophilic surfaces have a higher threshold velocity for splashing [20] and a significantly less oscillation time during droplet impact [22] than rigid surfaces.

A reduction in the contact time is beneficial for the development of self-cleaning and ice-proof surfaces. In comparison with the superhydrophilic/hydrophilic surface, the superhydrophobic/hydrophobic rigid surface can be used to reduce the contact time of a drop impact on the surface. Macrostructures or microstructures fabricated on the rigid superhydrophobic/hydrophobic surface can further promote rapid drop detachment, such as non-axisymmetric recoil on the macrostructure(ridge) superhydrophobic surface [24] and the pancake bouncing on the microstructure superhydrophobic surface [25]. Besides the rigid superhydrophobic/hydrophobic surface, the flexible

*Corresponding author. Tel.: +86-0431-85095196.
E-mail address: shench@jlu.edu.cn

superhydrophobic/hydrophobic surface also enable to significantly affect the droplet rebound and the droplet-surface contact time. Therefore, the distinct wetting dynamics of droplets impacting on a superhydrophobic/hydrophobic flexible surface needs to be further elucidated. Gart et al.[26] examined elastic beams with tunable surface wettability using a simple leaf model and discovered that wettable beams experienced much higher torque and bending energy than non-wettable beams. Wang et al.[27] developed a flexible, superhydrophobic surface (FS-surface) with a hierarchical structure composed of poly dimethyl siloxane (PDMS) and zinc oxide (ZnO). It was found that the soft micropapillae of the PDMS, which were covered by ZnO nanohairs, exhibited excellent elastic properties at low temperatures, which favored the rebound of droplets and provided excellent water repellency of the FS-surface, even in super-cooled environments. Vasileiou et al.[28] investigated the impact of droplets onto a superhydrophobic and low-density polyethylene (LDPE) food packaging film (12.5 μm thickness) and identified the rebound mechanism that was governed by substrate oscillation and velocity. This mechanism could take effect in a wide range of droplet viscosities, spanning from low- to high-viscosity fluids and even ice slurries. Vasileiou et al.[29] examined the interaction between droplets and an LDPE film treated with a superhydrophobic/hydrophobic nanocomposite. The results showed that, working synergistically with the surface microtexture or nanotexture, the flexibility of the film could be adjusted to increase the water repellency performance. Weisensee et al.[30] showed that the contact time of droplets impacting an elastic superhydrophobic surface (polymethylmethacrylate (PMMA)) was two times less than the contact time with equivalent rigid surfaces. It was found that the substrate oscillation and contact time of the droplet should have the same order of magnitude to achieve the lowest contact time. Weisensee et al.[31] investigated the impact dynamics of macroscopic water droplets (≈2.5 mm) on rigid and elastic superhydrophobic surfaces vibrating at 60-320 Hz and amplitudes of 0.2–2.7 mm. During forced vibration, the contact time was most sensitive to changes in the impact phase. The authors introduced the concept of a frequency-dependent critical impact phase, during which the contact time t_c transitioned rapidly from a minimum ($t_c \approx 0.5\ t_{c,th}$) to a maximum ($t_c \approx 1.6\ t_{c,th}$) ($t_{c,th}$ is the theoretical contact time when the droplet impacts the stationary hydrophobic surfaces)[4].

The thin, flexible films that were used in the aforementioned studies consisted of artificial materials, such as PDMS, LDPE, and PMMA. Natural materials, such as the wing features of small birds (e.g., the kingfisher), are flexible and hydrophobic/superhydrophobic and have excellent water repellency performance. An understanding of the combined effects of flexibility and superhydrophobicity of feathers on water repellency is highly informative for the design of water-repellant flexible substrates. Therefore, Zhang et al.[32] designed an elastic system that the superhydrophobic substrate is connected with a coil spring to reproduce the effect of droplets impacting a flexible surface. The authors found that downward movements of the elastic substrate significantly affected the droplet retraction and rebound, and reduced the contact time by up to 8.3% in the Weber number range from 17 to 32. Zhang et al.[33] experimentally investigated the droplet impact dynamics onto kingfisher wing feathers, which were highly flexible and near superhydrophobic. The result showed that, in the Weber number range from 1.06 to 36, the contact time of the water droplets on the flexible wing feather vane was significantly shorter than that on the rigid surface under the same superficial wetting conditions.

Experimental observations conducted by Zhang et al.[33] confirmed that, due to the flexibility of the kingfisher wing feather vane in its natural status, the rebound of the droplet was accelerated at a given Weber number. In this study, a numerical method is used to predict the droplet impact on a flexible surface with different inherent properties, such as the stiffness and the mass. The objective is to determine which property of the flexible surface has the largest influence on the rebound of the droplets. A one-dimensional simplified numerical method for simulating the fluid-structure interaction (FSI) is established to predict the impact of droplets on flexible surfaces. The feasibility of the numerical method is determined by comparing the simulation results to the experimental results. The contact times of droplets impacting elastic surfaces with different stiffness and masses and a rigid surface are compared, and finally, the relationships between the contact times and the actual frequencies and eigenfrequencies of the flexible surfaces are summarized.

2. Experimental tests for static and dynamic wetting characteristics of the flexible feather

2.1. Static wetting characteristic of the flexible kingfisher feather.

The kingfisher feather obtained from the inner wing and the scanning electron microscopy (SEM) images of the partially enlarged structure are shown in Fig.1 (a) and (b). The kingfisher feather samples used in the experiment were furnished by the Zoological and Botanical Garden of Changchun, Changchun, China. No birds were sacrificed specifically for this study. As shown in Fig. 1, the feather has an anisotropic structure. The cross-sectional views of the water droplet on the feather vane in the directions A-B and C-D are presented in Fig. 1 (c); the static apparent contact angles in different cross-sections are nearly the same. The static contact angles of the feather vane are in the range of $144.8° < \theta < 155.7°$[30].

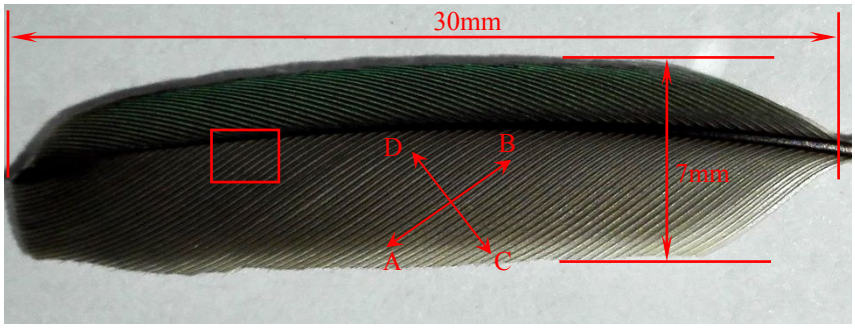

(a)

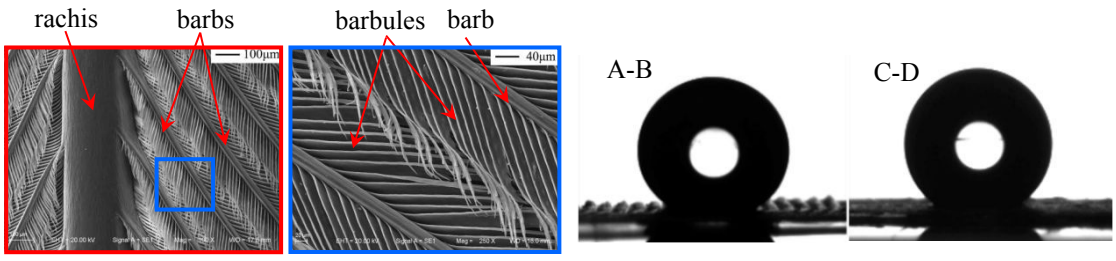

(b) (c)

Fig.1 Static characteristics of the kingfisher's wing feather. (a) A feather vane obtained from the inner wing. (b) SEM images of the partially enlarged feather structure. (c) Cross-sectional views of the static water droplet on a wing feather in different directions, i.e., A-B and C-D in (a).

2.2. Experimental apparatuses to observe droplets impact on the flexible kingfisher feather.

The experiments that droplets impacted on the rigid and flexible wing feather vanes were conducted, respectively. The rigid feather vane indicates that the feather is straightened from both ends, and the straight and flat feather vane was pasted on the flat glass substrate at both ends, using the double sided adhesive tape. The flexible feather vane was in the natural bending state and its one end was fixed on the glass substrate, using the double sided adhesive tape. The entire process of the droplet dynamic impact on the rigid and flexible feather vane were recorded by the high speed camera. The diameter of the water drop was approximately 2.056mm, and the ambient temperature for the experiments was 25℃. The concrete observation test steps and apparatuses were introduced in the references [10,32].

3. Numerical methods to predict the droplet impact on flexible surfaces.

3.1. Governing equations

The governing equations of the fluid phases, including the mass and moment equations, are given as follows:

$$\nabla \cdot \left(\boldsymbol{u} \text{-} \boldsymbol{u}_s \right) = 0 , \tag{1}$$

$$\frac{\partial \left(\rho \boldsymbol{u} \right)}{\partial t} + \nabla \cdot \left(\rho \boldsymbol{u} \left(\boldsymbol{u} - \boldsymbol{u}_s \right) \right) = \text{-} \nabla p_{rgh} \text{-} \boldsymbol{g} \cdot \boldsymbol{x} \nabla \rho + \nabla \cdot \mu \left(\nabla \boldsymbol{u} + \nabla \boldsymbol{u}^{\mathrm{T}} \right) + \boldsymbol{F}_\sigma , \tag{2}$$

with the fluid density ρ, the flow velocity $\boldsymbol{u}$, the velocity $\boldsymbol{u}_s$ for the moving mesh in Arbitrary Eulerian Lagrangian(ALE) framework, time t, the gravitational acceleration $\boldsymbol{g}$, the surface tension force term $\boldsymbol{F}_\sigma$ and the dynamic viscosity μ. In OpenFOAM [34] a modified pressure p_{rgh} is employed instead of the real pressure p, and it is given by

$$p = p_{rgh} + \rho \mathbf{g} \cdot \boldsymbol{x} , \tag{3}$$

where $\boldsymbol{x}$ is the vector from the origin.

3.2. Volume-of-fluid(VOF) method

Interface capturing scheme, includes Volume-of-fluid (VOF) and Level Set [35,36], are widely used in multiphase simulation in the one-fluid framework. VOF method is popular due to its simplicity. One of the drawbacks of the VOF is the smearing of interface, especially when the surface tension force dominates the problem. To overcome this issue, the fluid interface is sharpened by introducing the artificial compression term $\nabla \cdot \left(\left(1\text{-}\alpha \right) \alpha \boldsymbol{u}_{\mathrm{r}} \right)$ in the advection of volume fraction $\boldsymbol{u}_{\mathrm{r}}$ is the artificial compression velocity [10,37]. The advection equation for the interface capturing is given by

$$\frac{\partial \left(\alpha \right)}{\partial t} + \nabla \cdot \left(\alpha \boldsymbol{u} \right) + \nabla \cdot \left(\left(1\text{-}\alpha \right) \alpha \boldsymbol{u}_{\mathrm{r}} \right) = 0 \tag{4}$$

with the volume fraction of fluid phase α $(0 \le \alpha \le 1)$.

The continuum surface force (CSF) model is given by

$$\boldsymbol{F}_\sigma = \gamma \kappa \nabla \alpha , \tag{5}$$

with the coefficient of the surface tension γ, and the curvature of the fluid-gas interface κ, which is expressed as

$$\kappa = -\nabla \cdot \frac{\nabla \alpha}{|\nabla \alpha|}, \tag{6}$$

The density ρ and dynamic viscosity μ is mixed material properties with the volume fraction α, and they are given as,

$$\begin{aligned} \rho &= \alpha\rho_1 + (1-\alpha)\rho_2 \\ \mu &= \alpha\mu_1 + (1-\alpha)\mu_2 \end{aligned}, \tag{7}$$

with the subscript 1, 2 indicates the two component of fluid phases.

In order to suppress the non-physical parasitic currents(i.e., the numerical errors in the calculation, which primarily originate from an imbalance between the discrete surface tension force and the pressure-gradient terms in the aforementioned equation (2)) as much as possible [37,40], the volume fraction α is replaced by the smooth function $\tilde{\alpha}$ which is an area-weighted average based on interfacial phase volume fractions. The other details about the VOF approach with this smooth function above and the magnitude of the parasitic currents produced by this approach was specifically discussed in Ref. [10,37].

3.3. Models of Contact angle and partial slip velocity boundary at the moving contact line

On superhydrophobic and near superhyddrophobic surfaces, the difference between the advancing and receding contact angles is very small [9,26], and in general, the magnitude of the difference is approximately 5° for the scessile drop method. In this study, the dynamic contact angles are obtained from images acquired by a high-speed camera. The values of the advancing in the latter spreading and receding contact angle in the whole receding are both approximately 130°, i.e., the dynamic contact angle nearly remains in the value 130° from 1 ms after the drop has impacted the surface to the moment when the drop leaves the surface. The values obtained from the images are somewhat subjective and depend on the experience of the operator. It has been shown that this method of measuring the droplet contact angle results in errors of <±5° [41]. Therefore, it is difficult to determine small differences (approximately 5°) between the advancing and receding contact angles, and in the following simulation, both contact angles are set to 130°.

The partial slip velocity boundary at the moving contact line is adopted and the corresponding details were showed in Ref. [10].

3.4. Simplified fluid and structure interaction(FSI) model

The process of droplet impacting on the flexible feather is a typical fluid and structure interaction(FSI) problem [42,43], and in this paper, it is simplified to a one-dimensional mass-spring system, as shown in Fig. 2. The motion of the elastic system is described by the following ordinary differential equation:

$$m_e\ddot{y} + c\dot{y} + ky = F_y(t), \tag{8}$$

where y is the surface vertical displacement in the y-axis direction, m_e is the elastic system mass including the flat surface substrate and the spring, c is the spring damping coefficient, k is the spring stiffness, m_d is the mass of the droplet, and $F_y(t)$ is the droplet impacting force exerting on the flat surface substrate. The simplified undamped dynamic vibration model is adopted in the following

simulation, i.e., the effect of the spring damping coefficient c=0.

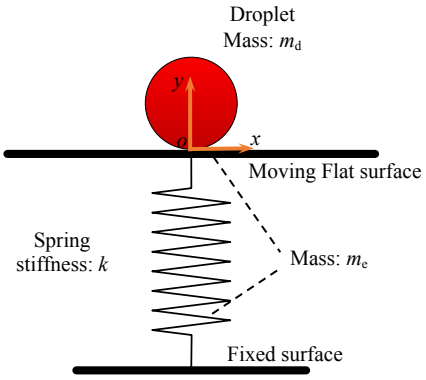

Fig. 2 Schematic of one-dimension simplified FSI model corresponding to the droplet impacting on the flexible feather surface

The total elastic system mass m_e including the flat surface and spring is equal to the mass of a kingfisher feather, which is approximately 0.01g. The modulus of the feather is approximately 2.5×10^9Gpa [44-46]. The bending style of the flexible feather vane which was fixed at one end in the experiment is as similar as a cantilever, and its stiffness is estimated according to the formula for the stiffness of the cantilever [30], i.e.,

$$k = 3EI / s^3 , \quad (9)$$

$$I = wh_s^3 / 12 , \quad (10)$$

where k is the stiffness of the one-end fixed feather cantilever, I is the area moment of inertia, E is the elastic modulus of the feather vane, w and h_s are the width and thickness of the feather vane, and s is the distance between the centerline of droplet impact and the fixed end. Based on the order of magnitude of the thickness, the values of width and length of the feather, i.e., w, h_s and s, are approximately equal to 10mm, 0.1mm and 10mm, respectively. Utilizing the parameters above, the estimated value of the stiffness of the elastic system in Fig.2 is about 6.2 N/m.

3.5. Grids for the geometric domain

The axisymmetric two-dimensional(2d) computational domain 5.4 mm×8.1 mm as shown in Fig. 3 (a), is adopted as the simulation domain for the droplet impact on the flat surface. In OpenFOAM, this domain is confined by two pieces of wedge patches, and the angle at the tip of the wedge domain is 5º. The square grid element is adopted in the whole computational domain, and the grid element is refined in the region which the impacting droplet flows across as shown in Fig. 3 (b). Fig. 4 shows the variations of the radius with time corresponding to the finest grid size 10μm, 5μm and 2.5μm, respectively. The curves corresponding to the finest grid size 5μm and 2.5μm are well coincident with each other, except the location at 9ms. In the latter receding(after 8ms), the curve corresponding to the finest grid size 10μm obviously deviates away from the other two curves. On the whole, the grid corresponding to the finest grid size 5μm conforms to the criteria of grid independence. Additionally, in order to reduce the computational cost as much as possible, the finest grid size 5μm is adopted in the following computation.

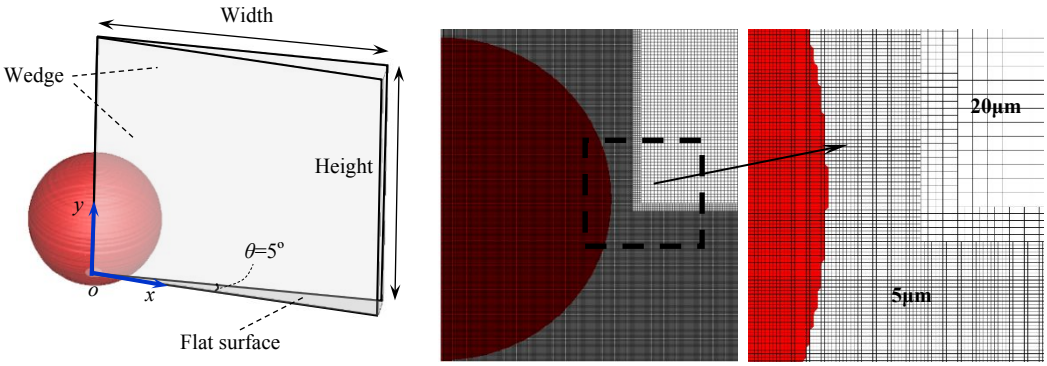

(a) (b)

Fig. 3 The computational domain and grids for the computation domain. (a) The 2d axisymmetric computational domain for droplets impacting on flat surface (b) The two-level hierarchical grids.

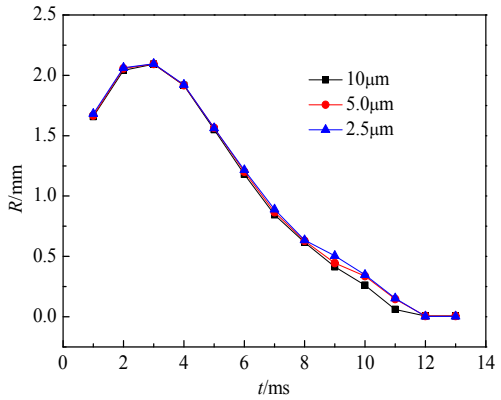

Fig. 4 Variations of the contact radius with time(drop impacting velocity 0.823 m/s) using the mesh with the finest grid size 10μm, 5μm and 2.5 μm, respectively.

Accompanying with the upward and downward movement of the moving flat surface in Fig. 2, i.e., the flat surface in Fig. 3 (a), the dynamic moving mesh is adopted. The mesh motion model in OpenFOAM is used to adapt to the displacement of the moving flat surface [47].

4. Results and discussion

4.1. Comparison of numerical results and experimental data

The droplet impact on the flexible surface was recorded by a high-speed camera, as shown in Fig. 5. At 4 s, the maximum compression deformation of the flexible feather occurs, and the lower surface of the feather vane touches the glass substrate. After 4 s, the drop begins to recede, and the deformed feather vane recovers gradually. At 9 s, the feather vane has recovered completely based on visual observation. At 11 s, the drop is about to leave the feather vane. Overall, the feather vane shows excellent performance, i.e., as the drop is spreading, the feather vane is compressed, and when the drop begins to recede, the feather vane recovers. This excellent response feature guarantees that when the drop is spreading, the flexible feather absorbs the drop's energy, and as the drop rebounds, the absorbed energy is returned back to the drop.

The impact of the drop on the flexible feather vane is reproduced by the numerical method

introduced in section 3. Corresponding to the ambient temperature in the experimental test, i.e., 25 °C, the dynamic viscosity, surface tension and density of water are, $\mu = 0.89 \times 10^{-3}$ kg·ms^{-1}, γ =0.072 N·m^{-1} and $\rho = 997$ kg·m^{-3}, respectively. The simulation results are shown in Fig. 6. At 4ms, the maximum deformation of the elastic surface occurs. After 4ms, the elastic surface begins to rebound. At 10ms, the drop is about to leave the surface. The drop rebound process predicted by the numerical results is about 1 ms faster than that of the experiment.

Additionally, the drop shapes in Fig. 5 are not axisymmetric due to the non-uniformity of the feather vane. As shown in Fig. 1 (c), the feather vane is anisotropic from the viewpoint of the distribution of rachis and barbs in Fig. 1 (b). There are two primary directional bending deformation. One is the rachis cantilever bending, and the other is the oblique barbs cantilever bending(A-B direction in Fig.1 (a)). These two directional deformations are superposed together to form the ultimate displacement of the feather vane. From the side views in Fig. 5, the maximum downward displacement obviously occurs at left side of the impacting droplet, and in top views, the drop deviates away from the rachis along the direction of the barbs. From the viewpoint of the drop shapes, the oblique barbs bending results in the gradual transformation of the circular drop into the conical drop, and the lower apex of the conical drop points to the barb direction as shown in the top views of Fig. 5 at 5ms and 6ms. This conical shape change caused by the oblique barbs cantilever bending should tend to reflect the non-axisymmetric shape change of the drop in the horizontal plane.

The one-dimension FSI numerical method in section 3 can not reproduce the non-axisymmetric shape of the impacting drop caused by the oblique deformation, i.e., the anisotropy of the feather bending is neglected. However, the overall shapes in the vertical longitudinal plane, predicted by the numerical method are still very similar to those shown in Fig. 6. In other words, for the drop impacting the flexible surface, the one-dimension FSI established in section 3 can effectively predict the droplet shape deformation and flexible surface displacement in the vertical direction.

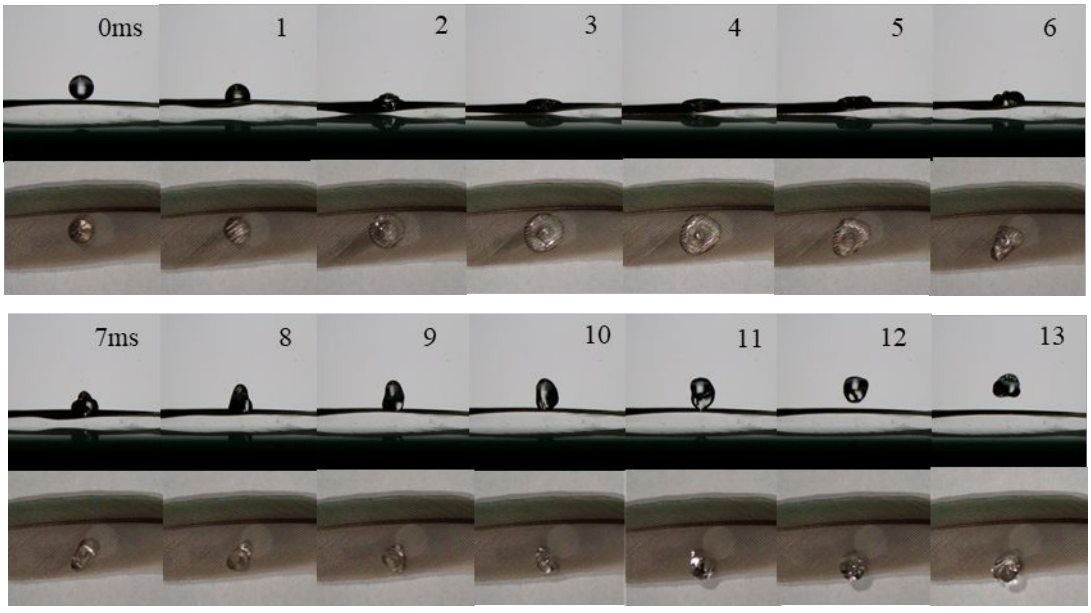

Fig.5 Snapshots of the droplet impact on the flexible feather vane recorded by the high speed camera(droplet impacting velocity vimp=0.87m/s).

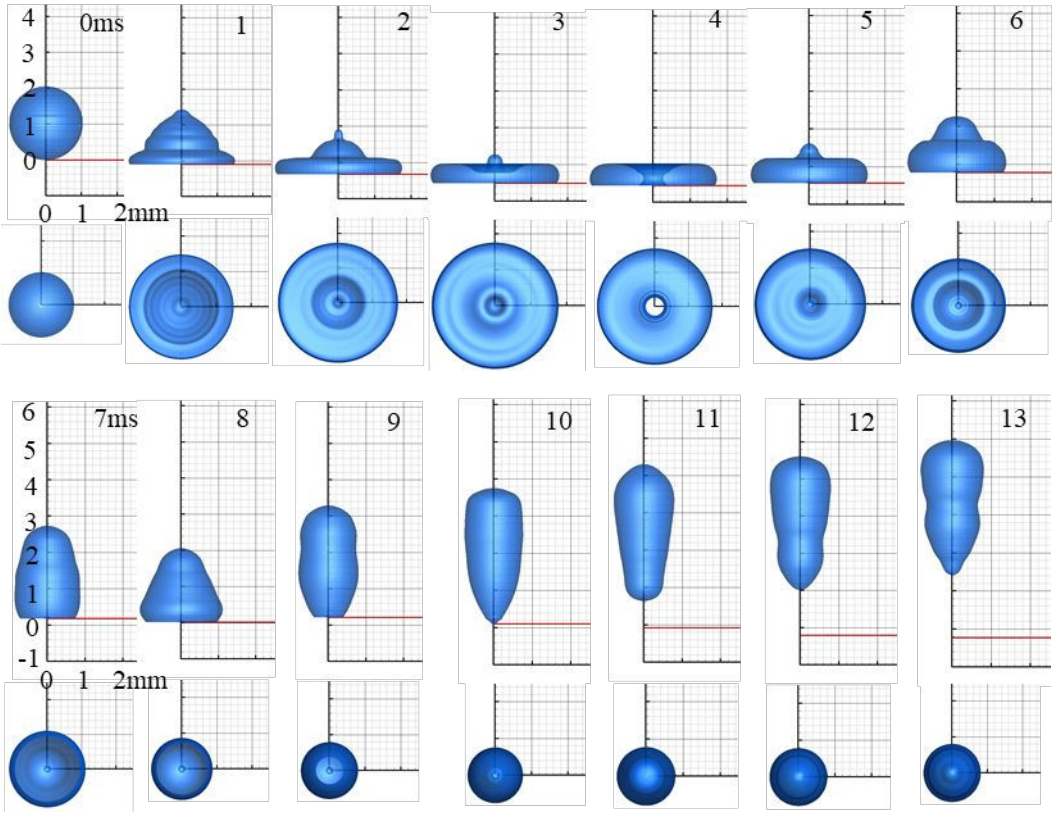

Fig.6 Snapshots of the water droplet impact on the flexible feather vane reproduced by the numerical method(droplet impacting velocity vimp=0.87m/s and the red line represents the elastic flat surface).

Fig. 7 shows the drop impact on a rigid surface, i.e., the feather vane whose two ends were fixed in the experiment. At 12 ms, the drop is about to leave the surface. On the flexible feather vane with one fixed end, the departure time is approximately 11 ms. The flexibility of the feather vane accelerates the rebound of the drop, unlike a rigid surface. Additionally, as the drop is about to leave the surface (from 9 ms to 12 ms), a secondary small drop is observed and it eventually separates from the top of the stretched drop. In contrast, no secondary drop is observed during the impact of the drop on the flexible feather vane.

Fig. 8 shows the drop impact on the rigid surface predicted by the numerical method. At 11 ms, the drop is about to leave the surface. The departure time of the drop from the flexible surface predicted by the numerical method is about 10 ms, as shown in Fig. 6. A comparison with the experimental data indicates that the numerical method provides an accurate representation of the acceleration of the drop as it leaves the flexible surface. Additionally, the predicted shapes of the drop are similar to those observed in the experiment. In other words, the numerical method provides good performance for predicting the impact of the drop on flexible and rigid surfaces and the drop rebound.

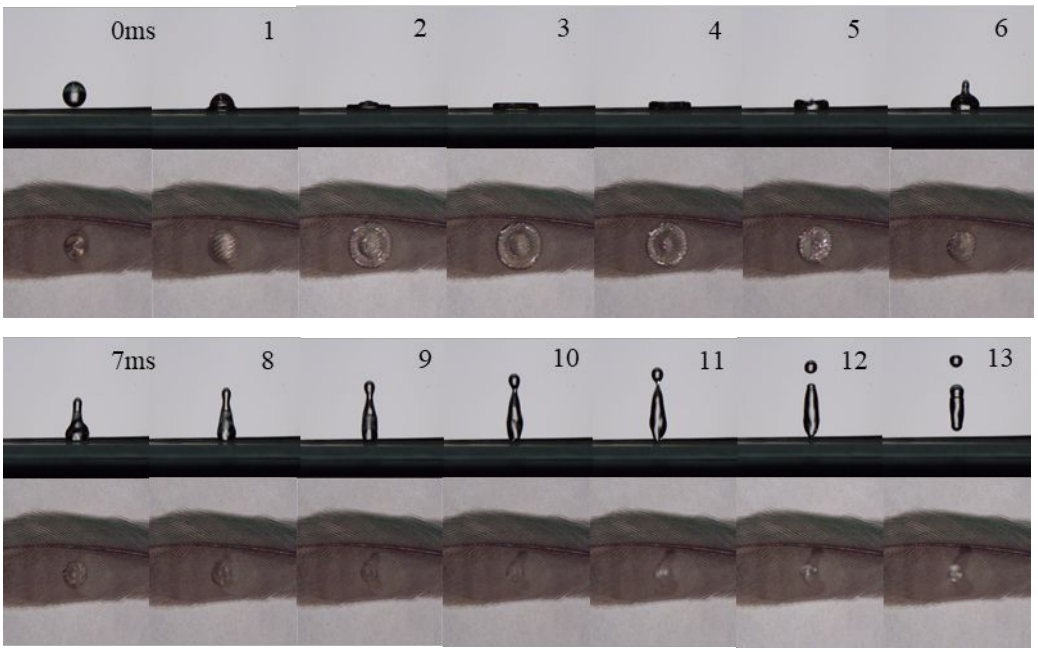

Fig.7 Snapshots of the droplet impact on the rigid feather vane recorded by the high speed camera(droplet impacting velocity vimp=0.98m/s).

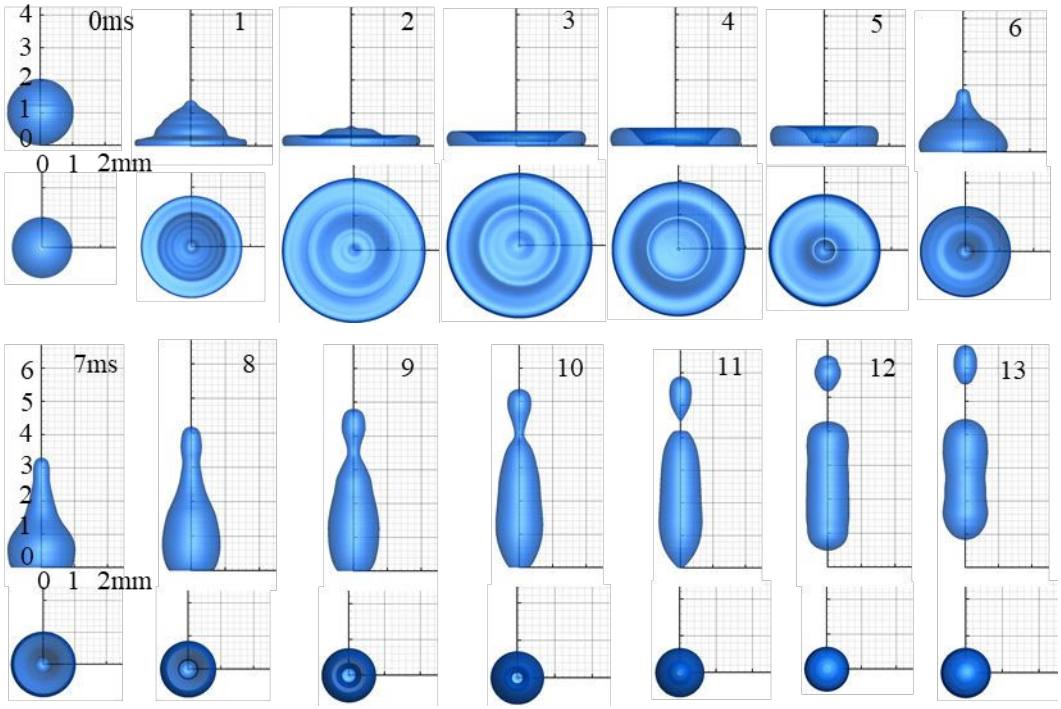

Fig.8 Snapshots of the water droplet impact on the rigid feather vane reproduced by the numerical method(droplet impacting velocity vimp=0.98m/s).

4.2. Effects of the eigenfrequencies of the elastic system and the droplet on the contact times

The numerical method is used to investigate the droplet impact for different elastic factors, i.e., the mass and the stiffness of the elastic system. The numerical results are used to determine the optimal properties of the elastic system to achieve the optimal acceleration during the drop rebound.

The effects of the elasticity on the droplet impact are analyzed from the viewpoint of the inherent frequencies(i.e., the eigenfrequencies) of the droplet and the elastic system. The eigenfrequency of the

water drop impacting rigid hydrophobic/superhydrophobic surfaces related to the surface tension coefficient γ is defined as[9,12]:

$$f_{\mathrm{d}} = \sqrt{\frac{8\gamma}{3\pi m_{\mathrm{d}}}} = \frac{\sqrt{2}}{\pi}\sqrt{\frac{8\gamma}{D^3\rho}}, \tag{11}$$

with the dynamic viscosity, water surface tension γ =0.072 N·m−1 and density ρ = 997 kg·m−3, respectively. According to the formula (11), the water viscosity doesn't affect the eigenfrequency of the water drop.

The eigenfrequency of the elastic system is defined as[12]:

$$f_{\mathrm{e}} = \frac{1}{2\pi}\sqrt{\frac{k}{m_{\mathrm{e}}}}, \tag{12}$$

with the total elastic system mass m_{e} and spring stiffness k.

Due to action of the external force which originates from the impacting droplet, the real vibrating frequency of the elastic system during the droplet impact should be different from its intrinsic eigenfrequency. In this paper, the real frequency of the elastic system in the actual vibrating process is defined as

$$f_{\mathrm{a}} = \frac{1}{2t_0}, \tag{18}$$

where t_0 denotes the time span from the start of the spring deform to the moment that the elastic surface returns to its equilibrium position for the first time after moving.

Table 1 shows the relationship between the eigenfrequencies of the elastic system and the contact times of the water drops impacting the rigid surfaces. The Weber number, $W_e=\rho v^2 D_0/\gamma$, ranges from 19.28 to 27.34, which corresponds to a velocity range of 0.823 to 0.98 m/s.

In the simulation, the dynamic advancing and receding contact angles are both 130°. The rigid surface that the water drop falls on is hydrophobic. Therefore, unlike for a superhydrophobic surface, the contact time of the water drop depends on the impact velocity. The contact times obtained from the numerical simulation increase with an increase in the impact velocity, as shown in Table 1. The contact time is lowest at the impact velocity of 0.98 m/s. In the subsequent discussion, it is taken as the primary comparison case for the drop impact on the elastic surface with the impacting velocity 0.87 m/s.

Table 1 Simulation results of the contact times of droplets impacting rigid surfaces

Case index	Droplet mass(g)	Impacting velocity vimp(m/s)	Weber number	Eigen frequency f(Hz)	Contact time τ(ms)
r-1	0.00453	0.98	27.34	116.12	11.11
r-2	0.00453	0.87	21.55	116.12	11.84
r-3	0.00453	0.823	19.28	116.12	12.01

Table 2 shows the contact times of the water drops impacting the flexible surfaces, the real frequencies and the corresponding eigenfrequencies of the elastic system with different masses and stiffnesses. Fig. 9 presents the variation of the contact times predicted by the numerical simulation versus the eigenfrequency of the elastic system. The range of mass of the elastic system me is from

2.5mg to 40mg, and the droplet impacting velocity vimp and the Weber number are 0.87m/s and 21.55, respectively. The mass of the impacting drop is 4.55mg(≈5mg), and the range of the elastic system mass me in Table 2 is approximately from half to eightfold that of the mass of the impacting drop, i.e., 2.5mg ~ 40mg.

As shown in Table 2 and Fig. 9, there are five groups of cases, and each group corresponds to one elastic system mass m_e. The five minimum contact times of these case groups appear at different eigenfrequencies 180.15Hz, 153.56Hz, 125.38Hz, 125.38Hz and 116.47Hz, respectively (i.e., case 3 for m_e = 2.5mg, case 8 for m_e = 5mg, case 15 for m_e = 10mg, case 21 for m_e = 20mg and case 25 for m_e = 40mg). The three eigenfrequencies for case8, case15 and case 21 with higher elastic system masses(m_e ⩾10mg) are much closer to the intrinsic eigenfrequency of the water drop impacting the rigid surface, i.e., 116.12 Hz in Table 1, and the two eigenfrequencies for case 3 and case 8 with lower elastic system masses(m_e<10mg) deviate farther away from the intrinsic eigenfrequency of the water drop.

As shown in Fig. 9, the values of these five minimum contact times become greater with the increment of the elastic surface masses. For case 25 with the m_e = 40mg, the value of contact time is even slightly greater than the contact time 11.11ms for cases r-1 in Table 1, i.e., the droplet impacting the rigid surface with the impact velocity 0.98m/s. The values of the contact times for case 3 with m_e = 2.5mg and case 8 with m_e = 5mg are low to 9.7 ms and 9.6ms, respectively, which are nearly 1.5ms smaller than that for case r-1 in Table 1.

Overall, the suitable combination of mass and stiffness of the surface will enhance the drop rebound, and a smaller mass system with higher eigenfrequency will decrease the minimum contact time.

Table 2 Numerical results of the contact times of droplets on the elastic surfaces and actual frequencies of the elastic system with different eigenfrequencies (me = 2.5mg ~ 40mg, vimp=0.87m/s, We=21.55).

Case index	Group index	Spring mass me(mg)	Spring stiffness k(N/m)	Eigen frequency fe(Hz)	Actual frequency fa(Hz)	Contact time τ(ms)
1	group-1	2.5	1.3375	116.47	51.37	12.66
2		2.5	2.325	153.56	64.72	10.21
3		2.5	3.2	180.15	76.62	9.75
4		2.5	4.3	208.83	86.56	11.94
5		2.5	5.35	232.94	98.65	12.58
6	group-2	5	2	100.71	55.11	12.80
7		5	2.675	116.47	61.26	10.96
8		5	4.65	153.56	74.73	9.60
9		5	6.2	177.32	90.70	11.95
10		5	9.3	217.17	108.23	12.10
11	group-3	10	1.3375	58.23	38.59	18.67
12		10	3.1	88.66	54.56	12.17
13		10	4.5	106.89	63.22	10.46
14		10	5.35	116.47	67.83	10.18
15		10	6.2	125.38	72.39	10.08
16		10	9.3	153.56	88.97	11.44
17		10	21.4	232.94	130.10	13.60

18	group-4	20	6.2	88.66	57.45	11.52
19		20	8	100.71	63.78	10.90
20		20	10.7	116.47	72.66	10.69
21		20	12.4	125.38	78.27	10.66
22		20	18.6	153.56	97.01	12.50
23	group-5	40	12	87.22	58.68	11.87
24		40	16	100.71	66.44	11.36
25		40	21.4	116.47	76.41	11.20
26		40	25	125.89	82.89	11.34
27		40	37.2	153.56	153.56	12.53

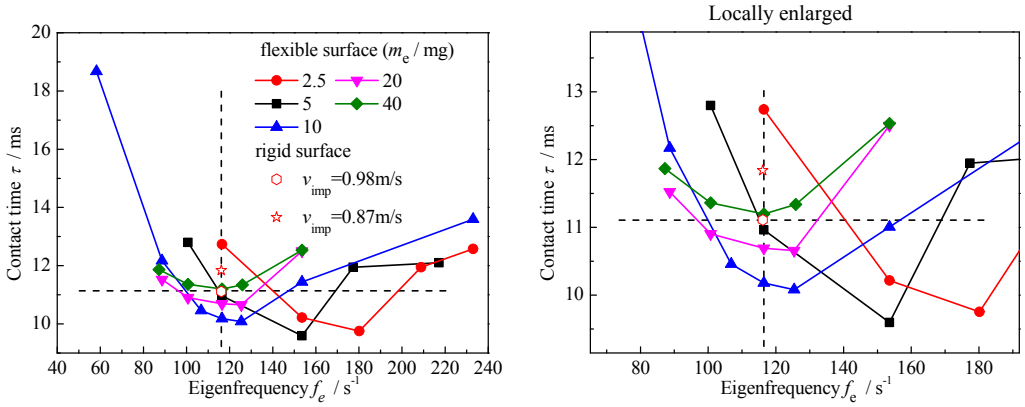

Fig. 9 The variation of the contact times predicted by the numerical simulation versus the eigenfrequencies of the elastic system.

For different elastic system masses, the eiginfrequencies corresponding to the minimum contact times are different as shown in Fig. 9, but due to the action of the external force which originates from the drop impact, the actual vibrating frequency of the elastic system should be different from its eigenfrequency. In comparison with the eigenfrequency of the elastic system, the actual frequency fa should influence the drop rebound more directly. Fig. 10 presents the variation of the contact times predicted by the numerical simulation versus the actual frequency of the elastic system. As shown in Fig. 10, it can be found that the actual vibrating frequencies of the elastic system with smaller contact times are all approximate at 75 Hz, no matter what the elastic system mass is, and in other words, the actual frequencies of the elastic systems which can effectively accelerate the drop rebound are approximate at 75 Hz.

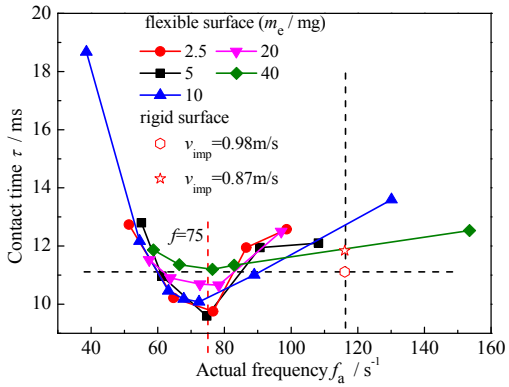

Fig. 10 The variation of the contact times predicted by the numerical simulation versus the actual frequencies of

the elastic systems.

In order to further reveal the effect of the actual vibration of the elastic system on the drop rebound, Fig. 11 presents the relationship between the impacting droplet contact radius and the deformation of the elastic system. In Fig. 11 (a), the eigenfrequencies of the three cases, i.e., case 3, case 8 and case 15 are 180.15Hz, 153.56Hz and 125.38Hz, and they are obviously different. However, from the viewpoint of the contact times in Table 2, all these three cases with obviously different eigenfrequencies can accelerate the drop rebound. Actually, the vibrating amplitude of the elastic system with the smaller mass is greater than that of the elastic system with the greater mass, so the difference of the actual vibrating frequencies between the elastic systems with higher and lower masses is not as much as the difference of their eigenfrequencies. Therefore, the actual frequencies of the three cases are 76.62Hz, 74.73Hz and 72.39Hz, respectively, and they are much closer to each other than their eigenfrequencies. Since the actual frequencies of the elastic system are close to effectively accelerating frequency 75Hz, as shown in Fig. 10, all these three cases with obviously different eigenfrequencies still can accelerate the drop rebound effectively.

In Fig. 11 (b), case 15, case 20 and case 25 have the relatively close eigenfrequencies, i.e., 125.38Hz, 116.47Hz and 116.47Hz, and their actual frequencies are 72.39Hz, 72.66Hz and 76.41Hz, which are all close to the effectively accelerating frequency, i.e.,75Hz. However, the actual vibrating amplitudes of these three cases are obviously different. Hereinto, the actual vibrating amplitudes of case 20 and case 25 with higher elastic system masses, are smaller than that of case 15 with relatively smaller elastic mass, and in other words, the effect of the vibration on the drop impact is weaker. Due to this weak influence on the drop impact, the contact times for these two cases are 10.69ms and 11.20ms, which are close to the contact time 11.11 on the rigid surface for case r-1 in Table 1.

In Fig. 11 (c), the eigenfrequencies of case 11 and case 17 are 58.23Hz and 232.94Hz, and their actual frequencies are 38.59Hz and 130.10Hz. At the droplet spreading stage, the time phases of the vibration peaks of the elastic systems for these two cases deviates far away from that of the summit of the maximum spreading radii, and it leads to that, at the droplet receding stage, the elastic surface not only can accelerate the drop receding, but also inhibit the drop retracting. Especially, the retraction rate of the elastic surface from maximum compression position is faster than the leaving rate of the triple line at the margin of the receding droplet, and it leads to the “chasing” effect that the radius of the droplet at the receding stage becomes larger reversely, as shown in the regions surrounded by the circles in Fig. 11 (c).

Fig.11 (d) shows the variations of the contact radii and the moving displacement of the elastic surface for the three cases with the elastic system mass me=2.5mg. The eigenfrequencies of case 1 and case 5 are 116.47Hz and 232.94Hz, and their actual frequencies are 51.37Hz and 98.65Hz. The actual frequencies of these two cases deviate away from that of case 3(76.62Hz) of which the actual frequency is approximately equal to the effectively accelerating value 75Hz. Of course, the contact times of case 1 and case 5 are 12.66ms and 12.58ms, and are greater that of case 3, i.e.,9.75ms. As similarly as the cases with greater elastic system mass me=10mg in Fig. 11 (c), there is also existing the obvious “chasing” effect in the receding process for case 1 and 5, and the moving of the elastic systems

can't effectively promote the drop rebounding.

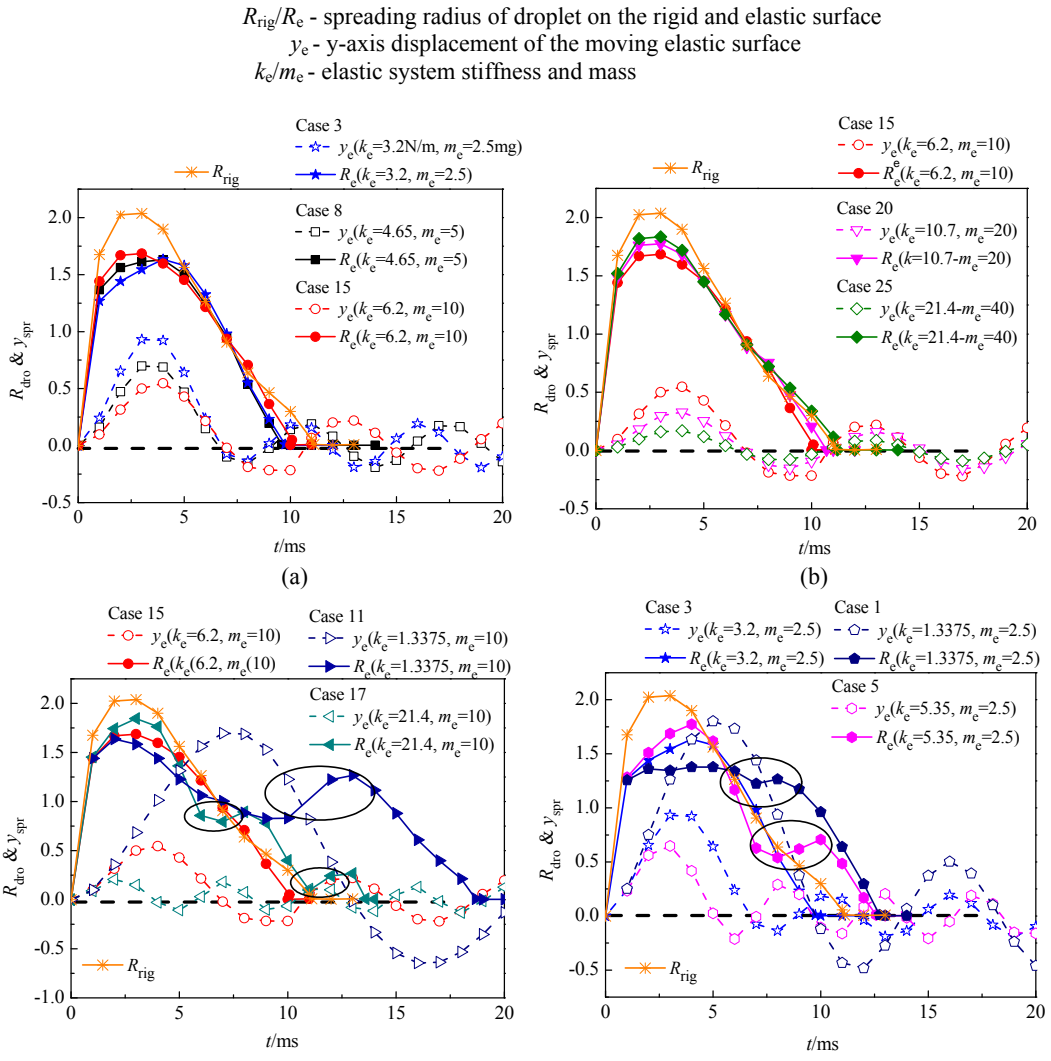

Fig. 11 The time variation of the contact radii of the spreading droplets and the deforming length of the stretched spring. R_{rig}(v_{imp}=0.98m/s, in Table 1) and R_e dictate spreading radius of droplet impacting on the rigid and elastic surface, y_e dictates the y-axis displacement of the moving surface in Fig. 2(here, the value y_e is positive when the spring system is compressed). (a)spring stiffness k_e=3.2N/m, spring mass m_e =2.5mg(case 3 in Table 2); k_e=4.65N/m, m_e =5mg(case 8 in Table 2) and case 15 k=6.2N/m, m_e=10mg. (b) k_e=6.2N/m, m=10mg(case 15 in Table 2); k_e=10.7N/m, m=20mg(case 20 in Table 2) and k_e=21.4N/m, m=40mg(case 25 in Table 2). (c) k_e=1.3375N/m, spring mass m_e =10mg(case 11 in Table 2) and k_e=6.2N/m, m_e =10mg(case 15 in Table 2) and case 17 k_e=21.4N/m, m_e=10mg. (d) k_e=1.3375N/m, m_e=2.5mg(case 1 in Table 2); k_e=3.2N/m, m_e=2.5mg(case 3 in Table 2) and k_e=5.35/m, m_e=2.5mg(case 5 in Table 2).

5. Conclusion

In this study, we investigated the effect of the inherent properties of an elastic system, i.e., the stiffness and the mass, on the rebound of droplets impacting a stationary flexible kingfisher feather vane. Experiments were conducted, and the simplified one-dimensional numerical model of the FSI was established to predict the impact of droplets on the elastic surface. The numerical simulation

results were validated by the experimental results. The validated numerical model was used to further predict the responses for cases with different masses and stiffnesses, and in this study, the magnitude of the mases and stiffnesses is approximately in the same order of magnitude of those of the flexible feather.

It was found that, for different elastic system masses m_e, the minimum contact times appears at the different eigenfrequencies. Overall, the suitable combination of mass and stiffness of the surface will enhance the drop rebound, and a smaller mass system with higher eigenfrequency will decrease the minimum contact time.

The effect of the elastic system with different masses on the promotion of droplet rebounding is clearly different, but during the droplet impacting process, the actual frequencies of the elastic systems which can accelerate the drop rebound are approximately at 75Hz, no matter what the elastic system mass is. If the actual frequency in the droplet impacting process deviates far away from this effective frequency value, i.e., 75Hz, the time phase difference between the vibration peaks of the elastic systems and the summit of the maximum spreading radii would be much greater. Due to this time phase difference, the elastic surface not only can accelerate the drop receding, but also inhibit the drop retracting.

Conflicts of interest

There are no conflicts of interest to declare.

Acknowledgement

This study was supported by, the National Key Research and Development Program of China (Grant No. 2018YFA0703300), the National Natural Science Foundation of China (Grant No. 51706084, 51875243, 51575227), the Science and Technology Development Program of Jilin Province (Grant No. 20180101319JC).

References

[1]C. Josserand, S.T. Thoroddsen. Drop impact on a solid surface. Annual Review of Fluid Mechanics. 2016, 48: 365-391

[2]K. Liu, L. Jiang. Bio-inspired self-cleaning surfaces. Annual Review of Materials Research. 2012. 42:231-63.

[3]D. Khojasteh, M. Kazerooni, S. Salarian, R. Kamali. Droplet impact on superhydrophobic surfaces: A review of recent developments. Journal of Industrial and Engineering Chemistry. 2016, 42: 1-14.

[4]D. Richard, C. Clanet, D. Quéré. Contact time of a bouncing drop. Nature.2002, 417: 811.

[5]J.B. Lee, D. Derome, A. Dolatabadi, J. Carmeliet. Energy budget of liquid drop impact at maximum spreading: numerical simulations and experiments. Langmuir. 2016, 32: 1279-1288.

[6]K. Yokoi, D. Vadillo, J. Hinch, I. Hutchings. Numerical studies of the influence of the dynamic contact angle on a droplet impacting on a dry surface. Physics of Fluids. 2009, 21, 072102.

[7]G.T. Liang, Y.L. Guo, Y. Yang, S. Guo, S.Q. Shen. Special phenomena from a single liquid drop impact on wetted cylindrical surfaces. Experimental Thermal and Fluid Science. 2013, 51: 18-27.

[8]G.T. Liang, Y.L. Guo, Y. Yang, S. Guo, S.Q. Shen. Special phenomena from a single liquid drop impact on wetted cylindrical surfaces. Experimental Thermal and Fluid Science. 2013, 51: 18-27.

[9]C. Antonini, A. Amirfazli, M. Marengo. Drop impact and wettability: From hydrophilic to superhydrophobic surfaces. Physics of Fluids. 2012, 24, 102104.

[10]C. Shen, C.C. Zhang, M.H. Gao, X.L. Li, Y. Liu, L.Q. Ren, A. S. Moita. Investigation of effects of receding contact angle and energy conversion on numerical prediction of receding of the droplet impact onto hydrophilic and superhydrophilic surfaces. International Journal of Heat and Fluid Flow. 2018, 74: 89-109.

[11]C.C. Zhang, Z.Y. Wu, Z. Z. Che, X.L Li. Y.H. Sun. L.Q. Ren. Liquid spreading on a pre-wetted biomimetic surface inspired by a dog's tongue. Science China Technological Sciences. 2016, 59(5):738-748.

[12]Y.H. Zheng, C.C. Zhang, J. Wang, Y. Liu, C. Shen, J.F. Yang. Robust adhesion of droplets via heterogeneous dynamic petal effects. Journal of Colloid and Interface Science. 2019, 557: 737-745

[13]C. Lee, Y. Nam, H. Lastakowski, J. I. Hur, S. Shin, A.L. Biance, C. Pirat, C.J. Kim, C. Ybert. Two types of Cassie-to-Wenzel wetting transitions on superhydrophobic surfaces during drop impact. Soft Matter. 2015, 11: 4592-4599.

[14]T.Y. Liu, C.J. Kim. Turning a surface superrepellent even to completely wetting liquids. Science. 2014, 346(6213): 1096-1100.

[15]Y.Q. Zu, Y.Y. Yan, J.Q. Li, Z.W. Han. Wetting behaviours of a single droplet on biomimetic Micro structured surfaces. Journal of Bionic Engineering. 2010, 7: 191-198.

[16]L. Moevius, Y.H. Liu, Z.K. Wang, and J. M. Yeomans. Pancake bouncing: simulations and theory and experimental verification. Langmuir. 2014, 30(43): 13021-13032

[17]H. Tan. Numerical study on splashing of high-speed microdroplet impact on dry microstructured surfaces. Computers & Fluids. 2017, 154(1): 142-166.

[18]A. M. Moqaddam, S. S. Chikatamarla, I. Karlin. Drops bouncing off macro-textured superhydrophobic surfaces. Journal of Fluid Mechanics. 2017, 824: 866-885.

[19]V. Vaikuntanathan, R. Kannan, D. Sivakumar. Impact of water drops onto the junction of a hydrophobic texture and a hydrophilic smooth surface. Colloids and Surfaces A: Physicochemical and Engineering Aspects. 2010, 369: 65-74.

[20]R. E. Pepper, L. Courbin, H. A. Stone. Splashing on Elastic Membranes: the Importance of Early-Time Dynamics. Physics of Fluids. 2008, 20: 082103.

[21]T. Gilet, J. W. Bush. The fluid trampoline: droplets bouncing on a soap film. Journal of Fluid Mechanics. 2009, 625: 167–203.

[22]S. Mangili, C. Antonini, M. Marengo and A. Amirfazli. Understanding the drop impact phenomenon on soft PDMS substrates. Soft Matter, 2012, 8: 10045-10054.

[23]D. Soto, A. B. D. Larivière, X. Boutillon, C. Clanet, D. Quéré . The force of impacting rain. Soft Matter, 2014, 10: 4929-4934.

[24]J.C. Bird, R. Dhiman, H.-M. Kwon, K.K. Varanasi. Reducing the contact time of a bouncing drop. Nature. 2013, 503: 385-388.

[25]Y.H. Liu, L. Moevius, X.P.Xu, T.Z Qian, J. M. Yeomans, Z.K. Wang. Pancake bouncing on superhydrophobic surfaces. Nature Physics, 2014, 10: 515-519.

[26]S. Gart, J. E. Mates, C. M. Megaridis, S. Jung. Droplet impacting a cantilever: a Leaf-raindrop system. Physical Review Applied. 2015, 3:044019.

[27]L.Wang , Q.H. Gong , S.H. Zhan , L. Jiang , Y.M. Zheng. Robust anti-icing performance of a flexible superhydrophobic surface. Advanced Materials. 2016, 28, 7729-7735.

[28]T. Vasileiou, T. M. Schutzius, D. Poulikakos. Imparting icephobicity with substrate flexibility. Langmuir, 2017, 33: 6708-6718.

[29]T. Vasileiou, J. Gerber, J. Prautzsch, T. M. Schutzius, D. Poulikakos. Superhydrophobicity enhancement through substrate flexibility. PNAS. 2016, 113(47): 13307-13312.

[30]P.B. Weisensee, J.J. Tian, N. Miljkovic, W. P. King. Water droplet impact on elastic superhydrophobic surfaces. Scientific Reports. 2016, 6:30328.

[31]P.B. Weisensee, J.C. Ma, Y.H. Shin, J.J. Tian, Y.J. Chang, W. P. Kin, N. Miljkovic. Droplet impact on vibrating superhydrophobic surfaces. Physical Review Fluids, 2017, 2: 103601.

[32]C.C. Zhang, Y.H. Zheng, Z.Y. Wu, J. Wang, C. Shen, Y. Liu, L.Q. Ren. Non-wet kingfisher flying in the rain: The water-repellent mechanism of elastic feathers. Journal of Colloid and Interface Science. 2019, 541: 56-64

[33]C.C. Zhang, Z.Y. Wu, X.M. Zhang, Y.L. Yue, J. Wang. Effect of feather elasticity of kingfisher wing on droplet impact dynamics. Journal of Bionic Engineering, 2018, 15: 731-740.

[34]H.G. Weller, G. Tabor, H. Jasak, C. Fureby. A tensorial approach to computational continuum mechanics using object orientated techniques. Computers in Physics. 1998,12(6):620-631.

[35]L. Yang, A.J. Gil, A.A. Carreño, J.Bonet. Unified one‐fluid formulation for incompressible flexible solids and multiphase flows: Application to hydrodynamics using the immersed structural potential method (ISPM). International Journal for Numerical Methods in Fluids, 2018. 86(1): 78-106.

[36]L. Yang. One-fluid formulation for fluid–structure interaction with free surface. Computer Methods in Applied Mechanics and Engineering 2018. 332: 102-135.

[37]D.A. Hoang, V.V. Steijn, L.M. Portela, M.T. Kreutzer , C.R. Kleijn. Benchmark numerical simulations of segmented two-phase flows in microchannels using the Volume of Fluid method. Computers & Fluids. 2013, 86: 28-36.

[38]A. Albadawi , D.B. Donoghue , A.J. Robinson, D.B. Murray b, Y.M.C. Delauré. Influence of surface tension implementation in volume of fluid and coupled volume of fluid with level set methods for bubble growth and detachment. International Journal of Multiphase Flow. 2013, 53: 11-28.

[39]M. Koch, C. Lechner, F. Reuter, K. Köhler, R. Mettina,W. Lauterborn. Numerical modeling of laser generated cavitation bubbles with the finite volume and volume of fluid method using OpenFOAM. Computers & Fluids. 2016, 126: 71-90.

[40]J.H. Ferziger, M. Peric. Computational methods for fluid dynamics. Berlin-New York: Springer Verlag, 1995.

[41]Š. Šikalo, H.D. Wilhelm, I. V. Roisman, S. Jakirliæ, C. Tropea. Dynamic contact angle of spreading droplets: Experiments and simulations. Physics of Fluids. 2005, 17, 062103.

[42]B.S. Carmo, S.J. Sherwin, P.W. Bearman, R.H.J.Willden. Flow-induced vibration of a circular

cylinder subjected to wake interference at low Reynolds number. Journal of Fluids and Structures. 2011, 27(4): 503-522.

[43]M. Kraposhin, K. Kuzmina, I. Marchevsky, Valeria Puzikova. Study of OpenFOAM® efficiency for solving fluid-structure interaction problems, in: Editors: J. M. Nóbrega, H. Jasak(Eds.), OpenFOAM® Selected Papers of the 11th Workshop. Springer International Publishing, Switzerland, pp. 465-479.

[44]T. Bachmann, J. Emmerlich, W. Baumgartner, J. M. Schneider, H. Wagner. Flexural stiffness of feather shafts: geometry rules over material properties. The Journal of Experimental Biology. 2012, 215: 405-415.

[45]J.L. Gao, G.Q. Zhang, L Guan, J.K. Chu, D.Y. Kong, Y.T. Bi. Structure and mechanical property of Asio Otus feather barbs. Key Engineering Materials. 2013, 562-565: 914-919.

[46]Y.J. Guo , J. Tong. Structures and mechanical properties of keratin materials. Transactions of the CSAE. 2004, 20(3): 266-270.(in Chinese)

[47]T. Maric, J. Höpken, K. Mooney. The OpenFOAM technology primer. Duisburg: Sourceflux, 2014.